

## Mesoporous Materials

Hierarchically Dual-Mesoporous TiO<sub>2</sub> Microspheres for Enhanced Photocatalytic Properties and Lithium Storage

Sa Xiao,<sup>[a]</sup> Yi Lu,<sup>[a]</sup> Xin Li,<sup>[a]</sup> Bing-Yu Xiao,<sup>[a]</sup> Liang Wu,<sup>[a]</sup> Jian-Ping Song,<sup>[a]</sup> Yu-Xuan Xiao,<sup>[a]</sup> Si-Ming Wu,<sup>[a]</sup> Jie Hu,<sup>[a]</sup> Yong Wang,<sup>[a]</sup> Gang-Gang Chang,<sup>[b]</sup> Ge Tian,<sup>\*[a]</sup> Silvia Lenaerts,<sup>[c]</sup> Christoph Janiak,<sup>[d]</sup> Xiao-Yu Yang,<sup>\*[a, e]</sup> and Bao-Lian Su<sup>[a, f]</sup>

**Abstract:** Hierarchically dual-mesoporous TiO<sub>2</sub> microspheres have been synthesized by a solvothermal process in the presence of 1-butyl-3-methylimidazolium tetrafluoroborate ([BMIm][BF<sub>4</sub>]) and diethylenetriamine (DETA) as co-templates. Secondary mesostructured defects in the hierarchical TiO<sub>2</sub> microspheres produce oxygen vacancies, which not only significantly enhance photocatalytic activity in the degradation

of methylene blue (1.7 times that with P25) and acetone (2.9 times that with P25), but are also beneficial for lithium storage. Moreover, we propose a mechanism to rationalize the role of this dual mesoporosity of the TiO<sub>2</sub> microspheres in enhancing molecular diffusion, ion transportation, and electronic transitions.

## Introduction

Mesoporous semiconductors enhance catalysis, photocatalysis, and electrical energy storage because the mesostructure provides the requisite highly accessible surface area, uniform porous structure, and an adjustable open framework.<sup>[1–10]</sup> Hierarchically mesoporous TiO<sub>2</sub> microspheres are therefore of great interest as high-performance photocatalysts<sup>[11–13]</sup> and high-

energy-storage host materials.<sup>[14]</sup> Indeed, hierarchical structures may exhibit very interesting properties, such as edge-active sites, unique multi-dimensional morphologies, a combination of micro- and nano-scales, shortened diffusion paths, and larger contact areas.<sup>[15–17]</sup> Monodispersed spherical TiO<sub>2</sub> structures can be successfully obtained by sol-gel methods by controlling the hydrolysis-condensation and the crystallization temperature.<sup>[18–21]</sup> However, many critical issues need to be addressed, such as the poor porous structure, the random crystal fusion, and the number of grain boundaries. This often results in a low level of active defects and rapid loss of electrons due to recombination or back-reaction. Oriented nanostructured TiO<sub>2</sub>, in the form of nanocrystals<sup>[18,22]</sup> and nanosheets,<sup>[19,23,24]</sup> has since been developed to improve the photocatalytic activity and/or energy storage capacity through the enhancement of charge transport and interparticle connection. Great progress has been made in the design of mesoporous single-crystal TiO<sub>2</sub>, which offers enhanced mobility and improved photoelectronic performance.<sup>[1]</sup> However, as a result of the large scale and highly crystalline nature of TiO<sub>2</sub>, a decrease in the number of surface defects/sites<sup>[25]</sup> and an unavailability of inner crystal lattices seems inevitable.<sup>[26]</sup> Recently, it was found that defect sites are of key importance to tune the functional properties of metal oxides, such as their electronic structure, charge transport, and catalytic performance.<sup>[22]</sup> Metal and oxygen vacancies are thought to be very important for engineering predictable semiconductors with remarkable properties. For example, substitutional impurities, including metal ions and doping atoms (such as H, N, or F), have been used to replace oxygen in order to generate oxygen site vacancies. Physical treatments, such as high-energy irradiation or oxygen-poor and oxygen-rich treatment have also proved effective for introducing oxygen/metal vacancies.<sup>[27,28]</sup> However, there have been few reports on nanosized defects, because the generation of nanoscale va-

[a] S. Xiao, Y. Lu, X. Li, B.-Y. Xiao, L. Wu, J.-P. Song, Y.-X. Xiao, S.-M. Wu, J. Hu, Y. Wang, Prof. G. Tian, Prof. Dr. X.-Y. Yang, Prof. B.-L. Su  
State Key Laboratory Advanced Technology for Materials Synthesis and Processing, and School of Materials Science & Engineering  
Wuhan University of Technology  
122, Luoshi Road, 430070 Wuhan (China)  
E-mail: tiange@whut.edu.cn

[b] Prof. G.-G. Chang  
School of Chemistry, Chemical Engineering and Life Science,  
Wuhan University of Technology  
122, Luoshi Road, 430070 Wuhan (China)

[c] Prof. S. Lenaerts  
Research Group of Sustainable Energy and Air Purification (DuEL)  
Department of Bioscience Engineering  
University of Antwerp, Antwerp (Belgium)

[d] Prof. C. Janiak  
Institut für Anorganische Chemie und Strukturchemie  
Heinrich-Heine-Universität Düsseldorf, 40204 Düsseldorf (Germany)

[e] Prof. Dr. X.-Y. Yang  
School of Engineering and Applied Sciences  
Harvard University, Cambridge, Massachusetts 02138 (USA)  
E-mail: xyyang@seas.harvard.edu

[f] Prof. B.-L. Su  
Laboratory of Inorganic Materials Chemistry (CMI)  
University of Namur  
61, rue de Bruxelles, 5000 Namur (Belgium)

Supporting information and the ORCID identification number for the author of this article can be found under:  
<https://doi.org/10.1002/chem.201801933>

cancies in single crystals is more difficult than atom-level defects.

Ionic liquids (ILs) have been developed as templates because of their unique templating behavior, based on the distinct polarizability of their head groups, leading to highly ordered pore systems.<sup>[17,29]</sup> In particular, ILs as environmentally benign non-volatile and thermally stable organic co-templates,<sup>[25]</sup> showing a significantly stronger tendency for self-aggregation and tolerance to perturbations compared with other templates, have been reported for the synthesis of hierarchical dual-mesoporous materials.<sup>[30,31]</sup>  $\text{BF}_4^-$  anions in ILs (designated as IL-F) can interact with  $\text{Ti}^{3+}$  cations because of a high F...Ti bonding energy, and act as templates to form a pore and/or defect structure at the nanoscale level. At the same time, decomposition and ready hydrolysis of  $\text{BF}_4^-$  will yield  $\text{F}^-$  anions and give rise to Ti...F atom-level defects.

Herein, we report a one-pot synthesis of hierarchically dual-mesoporous  $\text{TiO}_2$  microspheres (HDM- $\text{TiO}_2$ ) by a solvothermal process in the presence of 1-butyl-3-methylimidazolium tetrafluoroborate ([BMIm][ $\text{BF}_4$ ]) and diethylenetriamine (DETA) as co-templates. This dual mesoporosity of the HDM- $\text{TiO}_2$  microspheres plays an important role in enhancing molecular diffusion, ion transportation, and electronic transitions, which can greatly improve both the photocatalytic properties and the capacity for lithium storage.

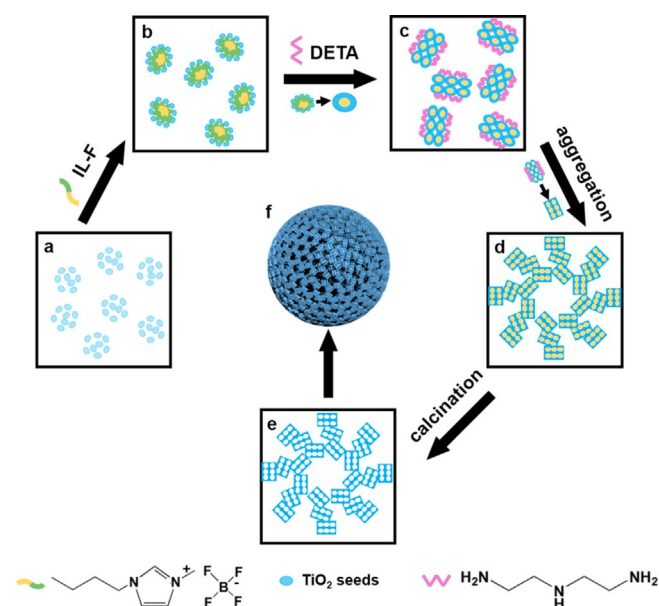


**Figure 1.** Schematic representation of the formation mechanism of HDM- $\text{TiO}_2$ : a cooperative self-assembly process in the presence of 1-butyl-3-methylimidazolium tetrafluoroborate ([BMIm][ $\text{BF}_4$ ]) and DETA as the structure-directing agent, showing the five procedures and the final 3D structure: (a)  $\text{TiO}_2$  seeds from the titanium precursor, (b)  $\text{TiO}_2$ -IL oligomers after adding the IL, (c)  $\text{TiO}_2$  nanoparticles formed with the aid of DETA, (d) formation of  $\text{TiO}_2$  microspheres by self-assembly of nanoparticles, (e) hierarchically dual-mesoporous  $\text{TiO}_2$  microspheres generated by calcination, and (f) corresponding 3D model.

## Results and Discussion

Figure 1 illustrates the fabrication process of HDM- $\text{TiO}_2$  and demonstrates the proposed mechanism whereby the morphology is formed by [BMIm][ $\text{BF}_4$ ] and DETA during the solvothermal synthesis procedure. The  $\text{TiO}_2$  precursor (Figure 1 a) is first mixed with [BMIm][ $\text{BF}_4$ ], whereupon  $\text{TiO}_2$ -IL oligomers (Figure 1 b) are formed due to the high F...Ti interaction energy and the templating effect of the IL.<sup>[26,32]</sup> During the solvothermal (propanol) process,  $\text{TiO}_2$ -IL oligomers are effectively controlled to grow along the [001] direction by DETA stabilization and aggregate to nanoparticles (Figure 1 c).<sup>[19]</sup> Because Ti...F bonds are stronger than the Ti...N bonds, the  $\text{TiO}_2$  nanoparticles contain and bind the [BMIm][ $\text{BF}_4$ ] template.<sup>[26]</sup> These nanoparticles are highly flexible and easily self-organize into hierarchical spheres (Figure 1 d). After calcination at 600 °C for 4 h, [BMIm][ $\text{BF}_4$ ] and DETA are removed (Figure 1 e) to finally afford the hierarchically dual-mesoporous structure (Figure 1 f).

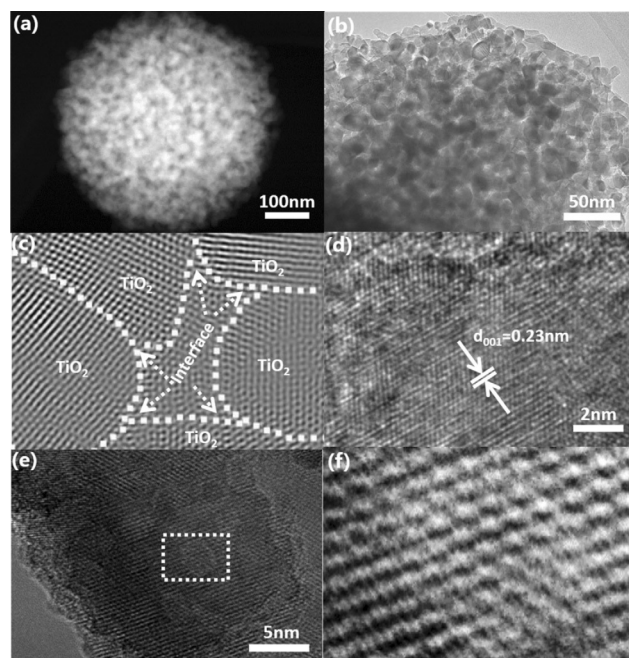


**Figure 2.** STEM image (a) and HRTEM image (b) of HDM- $\text{TiO}_2$ ; inverted FFT pattern (c) of HDM- $\text{TiO}_2$  (Figure S1 e), in which the dotted lines indicate the boundaries of the nanoparticles of HDM- $\text{TiO}_2$ ; HRTEM image (d) of some nanoparticles of HDM- $\text{TiO}_2$ ; HRTEM image (e), the inner hexagons represent the mesopores) of a nanoparticle of HDM- $\text{TiO}_2$ , and inverse FFT pattern (f) of HDM- $\text{TiO}_2$  (e).

The morphology and structure of HDM- $\text{TiO}_2$  were characterized by STEM and HAADF-TEM (Figure 2; HAADF = high-angle annular dark-field imaging). The STEM image of HDM- $\text{TiO}_2$  in Figure 2a indicates that the microspheres were built up from  $\text{TiO}_2$  nanoparticles. A TEM image of an HDM- $\text{TiO}_2$  microsphere (Figure 2b) shows that the nanoparticles had lengths in the range 15–25 nm and that large-sized mesopores were generated by aggregation of these nanoparticles. The  $\text{TiO}_2$  nanoparticles were bound together by an interconnecting amorphous/semicrystalline interface, this hetero-phase being heterogene-

ous and coherent on an atomic scale (Figure 2c). The 0.23 nm lattice spacing of the facets in Figure 2d corresponds to the (001) interplanar distance of  $\text{TiO}_2$ . An HRTEM image (Figure 2e) and an inverse fast Fourier transform (FFT) image (Figure 2f) of a single nanoparticle show the presence of secondary mesopores of size around 4 nm within the single-crystal nanoparticles. These mesopores were randomly dispersed within the nanoparticles and showed a hexagonal defect configuration (Figure 2e, f); these inner mesopores have no influence on the single-crystal structure. The Ti–F bonds of  $\text{TiO}_2$ -IL oligomers normally link with neighboring Ti–O bonds for crystal growth, which can preserve the single-crystal structure of nanoparticles, and the IL fragments of the  $\text{TiO}_2$ -IL oligomers act as templates to form the nanoscale defects.

HDM- $\text{TiO}_2$  and the samples for comparison (as-synthesized HDM- $\text{TiO}_2$ , and as-synthesized and calcined  $\text{TiO}_2$  without using IL-F as a template, termed HM- $\text{TiO}_2$ ) were also characterized. The XRD patterns (Figure S2) showed that all samples match well with the standard JCPDS no. (010-078-2486) of anatase  $\text{TiO}_2$ . Note that the XRD peaks of HDM- $\text{TiO}_2$  were sharper and narrower than those of HM- $\text{TiO}_2$ , indicating that the crystallization of the former was enhanced. Figure S3 in the Supporting Information shows the nitrogen adsorption–desorption isotherms and the pore size distribution curves (inset) of as-synthesized and calcined HDM- $\text{TiO}_2$  and HM- $\text{TiO}_2$ . The inset in Figure S3 and Table S1 show that, before calcination, the single pore distributions of HDM- $\text{TiO}_2$  and HM- $\text{TiO}_2$  were around 12 and 7 nm, respectively. After calcination, HDM- $\text{TiO}_2$  showed a dual pore size distribution (around 4 and 20 nm) due to removal of the IL-F template, in good accordance with the TEM data. Moreover, after calcination, the specific surface area of HDM- $\text{TiO}_2$  showed a large increase from 84 to  $131 \text{ m}^2 \text{ g}^{-1}$ , compared to a decrease for HM- $\text{TiO}_2$  (from 86 to  $57 \text{ m}^2 \text{ g}^{-1}$ ), due to

the secondary mesopores. The SAXS patterns of HDM- $\text{TiO}_2$  and HM- $\text{TiO}_2$  in as-synthesized form and after calcination at  $600^\circ\text{C}$  are collected in Figure S4. All of the samples showed a broad peak at low  $q$  values ( $q=4\pi\sin\theta/\lambda$ ), indicating a defined mesostructure.<sup>[33]</sup> After calcination, the peaks of HDM- $\text{TiO}_2$  and HM- $\text{TiO}_2$  shifted to lower  $q$  values and the unit cell parameter ( $a_0$ ) was changed from 25.6 to 28.3 nm and from 22.8 to 24.3 nm, respectively, coincident with the BET results. Figure S5 shows the Raman spectra of HDM- $\text{TiO}_2$ , HM- $\text{TiO}_2$ , and P25, which feature five Raman-active modes of Eg ( $146 \text{ cm}^{-1}$ ), Eg ( $198 \text{ cm}^{-1}$ ), B<sub>1g</sub> ( $399 \text{ cm}^{-1}$ ), A<sub>1g</sub> ( $519 \text{ cm}^{-1}$ ), and Eg ( $641 \text{ cm}^{-1}$ ). This result clearly indicates that the well-crystallized structure is preserved in the solvothermal synthesis. Figure S6 shows the FTIR spectra of HDM- $\text{TiO}_2$  and HM- $\text{TiO}_2$ , in which the broad absorption peaks at 3430 and  $1620 \text{ cm}^{-1}$  can be attributed to the stretching and bending vibrations of surface-adsorbed water and hydroxyl groups, respectively. HDM- $\text{TiO}_2$  shows stronger peaks at 3430 and  $1620 \text{ cm}^{-1}$ , indicating that it has more Ti–OH bonds and should degrade organic compounds more efficiently.<sup>[34]</sup> The absorption at around  $510 \text{ cm}^{-1}$  is assigned to the stretching vibration of Ti–O–Ti. The PL spectra of HDM- $\text{TiO}_2$ , HM- $\text{TiO}_2$ , and P25 in the wavelength range 350–550 nm under excitation light at 320 nm are shown in Figure S7. All of the samples give rise to five peaks, with those of HDM- $\text{TiO}_2$  being the weakest.<sup>[35]</sup> This observation indicates that HDM- $\text{TiO}_2$  with dual-mesoporous structure has a relatively low recombination rate of electrons and holes, which leads to high photocatalytic activity. Figure S8 shows the TGA curves of HDM- $\text{TiO}_2$  and HM- $\text{TiO}_2$  under an air flow at a temperature ramp of  $5^\circ\text{C min}^{-1}$ . HM- $\text{TiO}_2$  undergoes two main processes of weight loss, the first corresponding to the desorption of bound of water below  $280^\circ\text{C}$ , and the second corresponding to the loss of organics and the crystalline transformation between 280 and  $600^\circ\text{C}$ . HDM- $\text{TiO}_2$

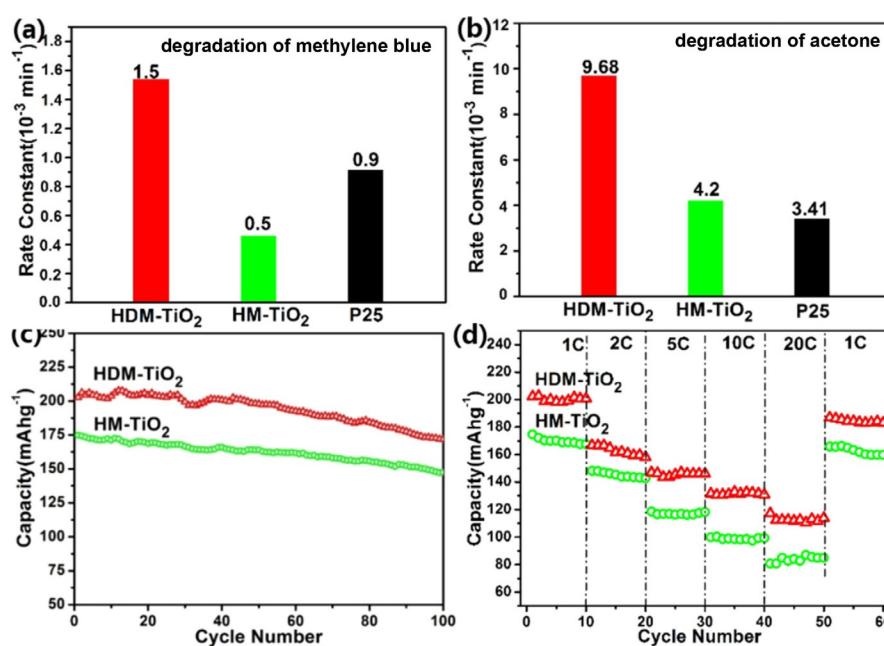


**Figure 3.** Photocatalytic rate constants for degradations of methylene blue (a) and acetone (b) with HDM- $\text{TiO}_2$ , HM- $\text{TiO}_2$ , and Degussa P25 under full light irradiation. Cycle performances of HDM- $\text{TiO}_2$  and HM- $\text{TiO}_2$  at a current density of 1 C (c) and various current rates of 1, 2, 5, 10, 20, and 1 C (d).

showed rapid weight loss between 480 and 600 °C owing to removal of the IL. Removal of the IL at 600 °C induced the formation of secondary defect mesopores.

The photodegradation of methylene blue (MB) under full light irradiation was investigated to evaluate the photocatalytic activities of HDM-TiO<sub>2</sub>, HM-TiO<sub>2</sub>, and P25, as shown in Figure 3a. Observing the degradation rate constants in Figure 3a, it is clear that HDM-TiO<sub>2</sub> exhibited the highest photocatalytic activity, with a rate constant of  $1.54 \times 10^{-3} \text{ min}^{-1}$ , which is about 1.7 times that of P25 ( $9.3 \times 10^{-4} \text{ min}^{-1}$ ) and 3.3 times that of HM-TiO<sub>2</sub> ( $4.6 \times 10^{-4} \text{ min}^{-1}$ ). Figure 3b displays the rate constants for acetone degradation under irradiation in the presence of HDM-TiO<sub>2</sub>, HM-TiO<sub>2</sub>, and P25. As in the case of MB degradation, HDM-TiO<sub>2</sub> again showed the highest photocatalytic activity, with a rate constant of  $9.68 \times 10^{-3} \text{ min}^{-1}$ , almost 2.9 times that of P25 ( $3.41 \times 10^{-3} \text{ min}^{-1}$ ) and 2.3 times that of HM-TiO<sub>2</sub> ( $4.2 \times 10^{-3} \text{ min}^{-1}$ ). HDM-TiO<sub>2</sub> exhibited higher photocatalytic activity in degrading both MB and acetone compared with HM-TiO<sub>2</sub> (single porosity) owing to its unique hierarchically dual mesoporosity, whereby the primary large-sized mesopores increase the contact area between the dye and the catalyst and facilitate the diffusion and transport of the dye therein, while the secondary small-sized mesopores induce more defects and active sites. Compared with MB, acetone is smaller and should diffuse more easily within the secondary pores. Hence, acetone photodegradation by HDM-TiO<sub>2</sub> and HM-TiO<sub>2</sub>, both having mesoporosity, is more efficient than that of nano-sized P25.

Figure 3c displays the high reversibility of the underlying electrochemical reactions over many charge–discharge cycles for HDM-TiO<sub>2</sub> and HM-TiO<sub>2</sub>. Remarkably, at a rate of 1 C, HDM-TiO<sub>2</sub> still retained an average capacity of 188 mA h g<sup>-1</sup> after 100 charge–discharge cycles. The rate performances of HDM-TiO<sub>2</sub> and HM-TiO<sub>2</sub> at current rates of 1–20 C are compared in Figure 3d. Notably, the reversible capacities of HDM-TiO<sub>2</sub> were maintained at 202 and 130 mA h g<sup>-1</sup> at 1 and 10 C, respectively. Even at a high current rate of 20 C, a high capacity of 125 mA h g<sup>-1</sup> could still be obtained, showing a high rate performance. Moreover, a capacity of 186 mA h g<sup>-1</sup> was maintained when the rate was reverted to 1 C. The cyclic voltammograms (CVs) of HDM-TiO<sub>2</sub> shown in Figure S9a display two well-defined current peaks corresponding to lithium-ion insertion and extraction at potentials of 1.7 V (Li insertion) and 2.1 V (Li extraction). Moreover, the second and third CV curves

almost overlap with the first, suggesting high reversibility and stability of the electrode in the following sweeps. Figure S9b presents the discharge–charge curves of HDM-TiO<sub>2</sub> at the 1st, 2nd, 10th, and 100th cycles at 1 C (170 mA g<sup>-1</sup>). It is evident that HDM-TiO<sub>2</sub> exhibits well-defined voltage plateaus, which can be observed at 1.7 V and 2.1 V during lithium-ion discharge and charge, in accordance with the CV curves. Figure S9c further displays the cycle performances of HDM-TiO<sub>2</sub> and HM-TiO<sub>2</sub> at 2 and 5 C, respectively. Remarkably, HDM-TiO<sub>2</sub> retains high average capacities of 160 and 132 mA h g<sup>-1</sup> after 100 cycles at rates of 2 and 5 C, whereas HM-TiO<sub>2</sub> shows average capacities of only 136 and 104 mA h g<sup>-1</sup>, respectively. Figure S9d shows the results of electrochemical impedance spectroscopy (EIS) analyses of HDM-TiO<sub>2</sub> and HM-TiO<sub>2</sub>. Nyquist plots are composed of a depressed semicircle (high-frequency region) and an inclined line (low-frequency region). The high-frequency region of the semicircle is a measure of the charge-transfer impedance ( $R_{ct}$ ). The HDM-TiO<sub>2</sub> electrode gave an  $R_{ct}$  value of 33 Ω, lower than that of HM-TiO<sub>2</sub> (72 Ω), due to its higher level of oxygen vacancies. Therefore, HDM-TiO<sub>2</sub> shows better lithium storage performance than HM-TiO<sub>2</sub> because it has dual mesopores with large pores and nanoscale defects, which decrease the diffusion distance of Li<sup>+</sup> and promote Li<sup>+</sup> insertion/removal.

To gain more information about the defects in HDM-TiO<sub>2</sub>, electron paramagnetic resonance (EPR) spectra were recorded at room temperature, as shown in Figure 4a. The EPR signals of Ti<sup>3+</sup>, O<sup>2-</sup>, and oxygen vacancies (VO) are seen at  $g = 1.960$ – $1.990$ ,  $2.020$ , and  $2.003$ , respectively.<sup>[36]</sup> As shown in Figure 4a, EPR peaks at around  $g = 1.986$  and  $2.011$  for HDM-TiO<sub>2</sub> correspond to the signals of Ti<sup>3+</sup> defects and oxygen vacancies, respectively, whereas no peak is seen for HM-TiO<sub>2</sub>. These findings indicate that the defect structure is caused by secondary mesopores, in good accordance with the defect structure revealed by the TEM images. In HDM-TiO<sub>2</sub>, Ti<sup>3+</sup> is produced by the presence of Ti–F–Ti bonds. As shown in Figure S10a,c, Ti<sup>4+</sup> peaks in the Ti2p spectrum of HDM-TiO<sub>2</sub> are found at 459.1 and 464.7 eV, attributable to Ti2p<sub>3/2</sub> and Ti2p<sub>1/2</sub>, respectively. There is no detectable Ti<sup>3+</sup> on the surfaces of any of the samples, probably due to the fact that Ti<sup>3+</sup> is easily oxidized by an appropriate oxidant, such as aerial O<sub>2</sub> and/or water-dissolved O<sub>2</sub>.<sup>[35]</sup> Besides the typical Ti–O–Ti peak at 529.8 eV for HM-TiO<sub>2</sub> (Figure S10d), HDM-TiO<sub>2</sub> shows an additional O1s peak at 531.8 eV, attributable to Ti–OH (Figure S10b). The F1s XPS

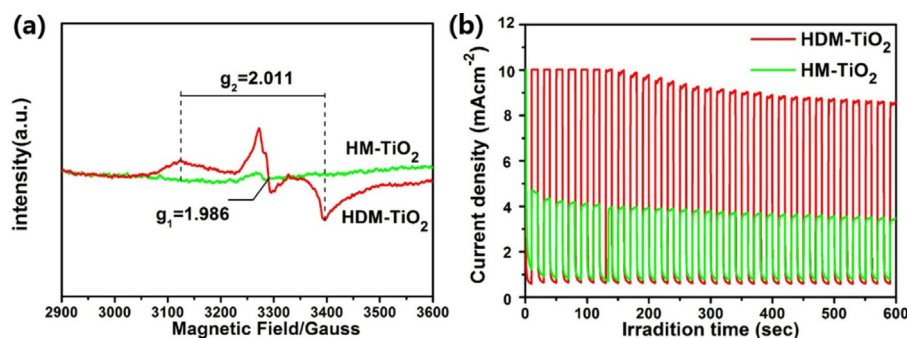


Figure 4. EPR spectra (a) and photoelectrochemical (PEC) reaction (b) of HDM-TiO<sub>2</sub> and HM-TiO<sub>2</sub>.

data of HDM-TiO<sub>2</sub>, as-synthesized and calcined at 600 °C, are shown in Figure S10e,f. A clear F 1s peak at 684.1 eV is seen for as-synthesized HDM-TiO<sub>2</sub> before calcination (Figure S10e), which can be assigned to a typical F species having a Ti–F bond.<sup>[35]</sup> After calcination, the F species (Figure S10f) is removed and the peak disappears, in good agreement with the TGA data (Figure S8). The stronger oxygen vacancy signal is in good agreement with the EPR analysis. It reveals that HDM-TiO<sub>2</sub> has more oxygen vacancies than HM-TiO<sub>2</sub>. With the removal of F and the loss of O atoms, more oxygen vacancies appear. As a measure of the photocatalytic activity, the photoelectrochemical (PEC) reaction is displayed in Figure 4b for HDM-TiO<sub>2</sub> and HM-TiO<sub>2</sub>. The photocurrent density measured at 0.5 V (vs. Ag/AgCl) for HDM-TiO<sub>2</sub> (1.5 mA cm<sup>-2</sup>) was found to be 2.5 times that of HM-TiO<sub>2</sub> (0.94 mA cm<sup>-2</sup>). The high photocurrent density observed for HDM-TiO<sub>2</sub> can be attributed to the presence of more oxygen vacancies. This indicates that introducing defect states can be very beneficial for the separation of carriers and slightly decreases the conduction band of TiO<sub>2</sub> (Figure S11 and Table S1).<sup>[37]</sup>

Figure 5 shows the proposed mechanism of the photocatalytic degradations of MB and acetone in HDM-TiO<sub>2</sub> and lithium storage therein. The nanoscale defect structure directly results in the presence of oxygen vacancies, which slightly decrease the band gap (core part of Figure 5). Electrons can transfer from both the valence band and oxygen vacancy state to the conduction band of HDM-TiO<sub>2</sub>.<sup>[37]</sup> This is beneficial to both electronic transitions during photocatalysis and high electron conduction during insertion/removal of lithium ions. The left-hand-side of Figure 5 (light-blue area) shows the performance of HDM-TiO<sub>2</sub> in degrading acetone and MB. With the response

of HDM-TiO<sub>2</sub> under UV light excitation, electrons can easily leap from both the valence band and oxygen vacancies to the conduction band, and the “free” electrons in the defective crystal may take the places occupied by O<sup>2-</sup> anions in the regular lattice.<sup>[27]</sup> This way of generating photoelectrons would also form holes, which could convert H<sub>2</sub>O and OH<sup>-</sup> into highly reactive ·OH and thereby degrade dye molecules. In the present case, the large-sized pores in HDM-TiO<sub>2</sub> promote the diffusion of dye molecules between the TiO<sub>2</sub> nanoparticles and enhance contact and reaction area. The secondary defects in the TiO<sub>2</sub> nanoparticles not only enlarge the contact area, but also provide more oxygen vacancies, which accelerate electron transfer and enhance the photocatalytic activity. The lithium-ion storage mechanism of HDM-TiO<sub>2</sub> is illustrated in the right-hand part of Figure 5 (dark-blue area). As described for dye molecule diffusion, the dual porous structure can reduce the diffusion distance of the electrolyte, facilitating the insertion of lithium ions and electron conduction. Moreover, oxygen vacancies caused by the secondary porosity can enhance the electrical conductivity, significantly accelerate electron transfer, and boost the uptake and release of Li<sup>+</sup> ions.

## Conclusions

In summary, a facile co-templating approach to obtain hierarchically dual-mesoporous TiO<sub>2</sub> microspheres has been presented. The utilization of IL-F not only leads to secondary mesopores in hierarchical TiO<sub>2</sub> microspheres, but also significantly increases the specific surface area and produces oxygen vacancies. Our results show that HDM-TiO<sub>2</sub> offers enhanced photocatalytic activity for the degradation of MB and acetone, and also displays high performance for lithium storage. Therefore, this work provides a promising means of introducing secondary mesopores in hierarchically mesoporous TiO<sub>2</sub> by the use of an ionic liquid and provides new insights for the design of hierarchically dual-mesoporous TiO<sub>2</sub> with nanoscale defects and having enhanced photocatalytic activity and lithium storage capacity.

## Experimental Section

### Chemicals

Diethylenetriamine (DETA; 99%), titanium isopropoxide (TTIP; 95%), propanol (95%), and acetone (98%, GC) were provided by Shanghai Aladdin Biochemical Technology Co., Ltd. 1-Butyl-3-methylimidazolium tetrafluoroborate [BMIm][BF<sub>4</sub>] (≥ 99%) was provided by Lanzhou Greenchem ILs. All chemical reagents were utilized as received without further purification, and distilled water was used in all experiments.

### Synthesis

In a typical procedure, DETA (24 μL) and [BMIm][BF<sub>4</sub>] (1 mL) were mixed with propanol (35 mL) in a 50 mL Teflon-lined stainless steel autoclave. After sealing, the contents were stirred for 10 min, whereupon TTIP (2 mL) was added to the mixture. After stirring for a further 10 min, the autoclave was placed in an oven and kept at 180 °C for 24 h. After cooling to room temperature, the sample

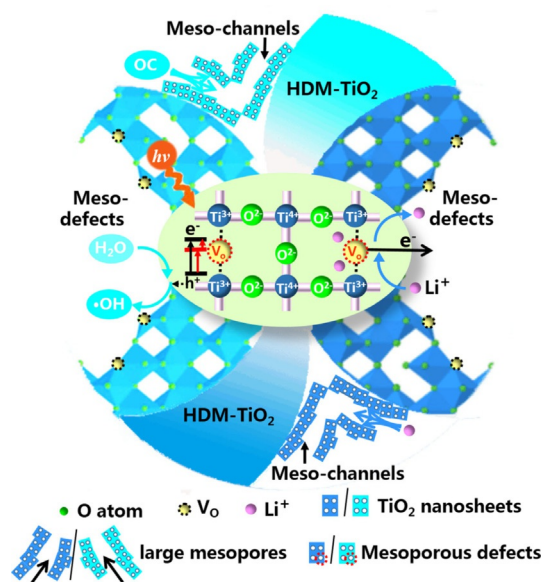


**Figure 5.** The mechanisms of the OC (organic compounds, including photocatalytic MB and acetone) degradation reaction (left) and lithium-ion storage (right) in HDM-TiO<sub>2</sub>. The light-blue part on the left and the dark-blue part on the right depict the mechanisms of photocatalytic performance and lithium-ion storage, respectively; the core part depicts a ball-and-stick model of oxygen vacancies and Ti<sup>3+</sup>.

was obtained through centrifugal separation, washed three times each with water and ethanol, and dried at 70 °C for 12 h. The dried sample was finally calcined at 600 °C in air for 4 h to obtain hierarchically dual-mesoporous TiO<sub>2</sub> microspheres (HDM-TiO<sub>2</sub>). [BMIm][BF<sub>4</sub>] was replaced by water to synthesize hierarchical TiO<sub>2</sub> microspheres (HM-TiO<sub>2</sub>) for comparison.

### Characterization

Sample morphologies were inspected by means of a field-emission scanning electron microscope (Hitachi S-4800, 5 kV) and a transmission electron microscope (TEM, JEOL-2100F). Phase and crystal size were determined by X-ray diffraction analysis (D8 Advance XRD) employing Cu<sub>Kα</sub> radiation, operated at a tube current of 40 mA and a voltage of 40 kV at a scan rate of 0.1° (2θ) s<sup>-1</sup>. Data were collected in the range 10° to 80°. SAXS patterns were measured by means of an SAXSess mc2 (Anton Paar) apparatus, equipped with a Cu tube (λ = 1.54 Å) and operating at 40 kV and 50 mA. BET specific surface area was measured by N<sub>2</sub> adsorption (TriStar TM II 3020). Measurement was commenced after the samples had been degassed at 120 °C for 12 h. UV/Vis diffuse-reflectance spectra (UV/Vis DRS) were obtained on a UV/Vis spectrophotometer (UV-2550). X-ray photoelectron spectroscopy (XPS) was performed with a PHI 5000 Versa Probe system with monochromatic Al<sub>Kα</sub> X-rays to determine the surface elements, compositions, and chemical states of the samples. Fourier-transform infrared spectra (FTIR) of the samples were measured with a Nicolet Avatar 360 FTIR spectrometer from samples in conventional KBr pellets. Photoluminescence (PL) spectra were obtained with an LS55 spectrometer (Perkin-Elmer) with an excitation wavelength of 320 nm. Electron paramagnetic resonance (EPR) spectra were measured on an EMX 10/12 spectrometer working in the X-band region at room temperature with an EPR quartz probe cell. Raman spectra were measured on an Invia Raman Microscope with a 632.8 nm laser as the excitation source, under ambient conditions. Thermogravimetric analysis (TGA) was performed under air flow at a heating rate of 5 °C min<sup>-1</sup>.

### Photocatalytic activity evaluation

Methylene blue (MB) was chosen as a model pollutant to conduct photocatalytic activity tests. Typically, 0.02 mg mL<sup>-1</sup> MB solution (100 mL) and catalyst (20 mg) were placed in a beaker. The distance between the solution and a 300 W xenon lamp (PLS-SXE300C, Beijing Trusttech Co., Ltd.) with a 200–800 nm UV output was fixed at 10 cm. The solution was stirred in the dark for 30 min until the concentration of MB remained steady, indicating its adsorption saturation. During the photocatalytic reaction, aliquots (2 mL) of the suspension were withdrawn at intervals of 2.5 min. The catalyst was removed from the suspension by centrifugation. The remaining pure liquid was tested by UV/Vis spectrophotometry. In order to test the vapor-phase catalysis of the samples, acetone was chosen as a model pollutant. In a typical experiment, photocatalyst (10 mg) was added to ethanol (2 mL) in a glass reactor. The mixture was sonicated for 30 min to obtain a suspension, which was then concentrated to dryness at 80 °C for 12 h. The catalyst was thereby deposited on the bottom of the reactor in the form of a thin film. The reactor was placed in a sealed vessel, and then acetone (5 μL) was injected through a valve to give an initial concentration of 600 ppm. The mixture was left for 30 min to allow equilibration of the acetone concentration. A 300 W, 200–800 nm UV lamp (2 cm above the dishes) (Perfect Light PLS-SXE 300) was then switched on. Aliquots (100 μL) of gas were sampled from the

system by means of a syringe at intervals of 10 min and analyzed with a gas chromatograph (GC 900C).

### Lithium storage

Lithium storage measurements were carried out using a two-electrode Swagelok cell and regarding lithium metal as the reference electrode and the counter electrode. The working electrode was composed of active material (e.g., HDM-TiO<sub>2</sub>), a conductive agent (carbon black, Super-P-Li), and a polymer binder [poly(vinylidene difluoride), PVDF, Aldrich] in a weight ratio of 70:20:10. The electrolyte was 1.0 M LiPF<sub>6</sub> in a 50:50 (w/w) mixture of ethylene carbonate and diethyl carbonate. Cells were assembled in an Ar-filled glove-box with < 1.0 ppm moisture and oxygen. Cyclic voltammetry (1–3 V, 0.2 mV s<sup>-1</sup>) was performed on an electrochemical workstation (CHI 660C). Charge/discharge tests were performed on a Neware battery tester at different current rates (1 C) (170 mA g<sup>-1</sup>) in the voltage range 1–3 V. Electrochemical impedance spectra (EIS) were measured on an electrochemical workstation (Autolab PGSTAT302N) in the frequency range from 100 kHz to 0.01 Hz with an amplitude of 5 mV. All electrochemical measurements were carried out at room temperature.

### Photocurrent measurements

Photocurrents were measured using a Pt foil as the counter electrode and an Ag/AgCl reference electrode at 0.5 V potential bias on a CHI 660D electrochemical workstation (Chenhua Instruments, Shanghai, China) under a 300 W, 200–800 nm UV lamp (2 cm above the dishes) (Perfect Light FX 300) in a conventional three-electrode system. Catalyst (5 mg) and Nafion<sup>®</sup> solution (100 μL, 0.5 wt %) were firstly dispersed in a mixed solvent of water/ethanol (1 mL, 1:1, v/v) and sonicated for at least 30 min to form a homogeneous ink. The working electrode was obtained by drop-casting the above ink (50 μL) onto FTO glass with a surface area of 1 cm<sup>2</sup>.

### Acknowledgements

This work is supported by the National Key R&D Program of China (2017YFC1103800), the Program for Changjiang Scholars and Innovative Research Team in University (IRT 15R52), the National Natural Science Foundation of China (U1662134, U1663225, 51472190, 51611530672, 51503166, 21706199, 21711530705), the International Science & Technology Cooperation Program of China (2015DFE52870), the Natural Science Foundation of Hubei Province (2016CFA033, 2017CFB487), the Open Project Program of State Key Laboratory of Petroleum Pollution Control (PPC2016007), and the CNPC Research Institute of Safety and Environmental Technology.

### Conflict of interest

The authors declare no conflict of interest.

**Keywords:** energy storage · hierarchical dual-mesoporous TiO<sub>2</sub> · ionic liquids · mesostructured defects · photocatalysis · template synthesis

[1] E. J. W. Crossland, N. Noel, V. Sivaram, T. Leijtens, J. A. Alexander-Webber, H. J. Snaith, *Nature* **2013**, *495*, 215–219.

- [2] X.-Y. Yang, L. Alexandre, L. Arnaud, G. Tian, B.-L. Su, *Chem. Commun.* **2011**, 47, 2763–2786.
- [3] X.-H. Li, J. Lian, M. Lin, Y.-T. Chan, *J. Am. Chem. Soc.* **2011**, 133, 672–675.
- [4] X.-F. Li, T.-X. Fan, H. Zhou, S.-K. Chow, W. Zhang, D. Zhang, Q.-X. Guo, H. Ogawa, *Adv. Funct. Mater.* **2009**, 19, 45–56.
- [5] Y. Lu, X. Cheng, G. Tian, H. Zhao, L. He, J. Hu, S.-M. Wu, Y. Dong, G.-G. Chang, S. Lenaerts, S. Siffert, G. Van Tendeloo, Z.-F. Li, L.-L. Xu, X.-Y. Yang, B.-L. Su, *Nano Energy* **2018**, 47, 8–17.
- [6] J.-C. Rooke, T. Barakat, M.-F. Finol, P. Billefont, G. De Weireld, Y. Li, Y. R. Cousin, J.-M. Giraudon, S. Siffert, J.-F. Lamonier, *Appl. Catal. B* **2013**, 142, 149–160.
- [7] Y. Gao, B.-F. Fan, R. Feng, C.-L. Ye, X.-J. Wei, J. Liu, X.-H. Bu, *Nano Energy* **2017**, 40, 462–470.
- [8] S.-Y. Gao, K.-R. Geng, *Nano Energy* **2014**, 6, 44–50.
- [9] Z.-K. Zheng, B.-B. Huang, J. Lu, X.-Y. Qin, X.-Y. Zhang, Y. Dai, *Chem. Eur. J.* **2011**, 17, 15032–15038.
- [10] Y. Dong, S.-Y. Chen, Y. Lu, Y.-X. Xiao, J. Hu, S.-M. Wu, Z. Deng, G. Tian, G.-G. Chang, J. Li, S. Lenaerts, C. Janiak, X.-Y. Yang, B.-L. Su, *Chem. Asian J.* **2018**, 13, 1609–1615.
- [11] C.-P. Han, D. Yang, Y.-K. Yang, B.-B. Jiang, Y.-J. He, M.-Y. Wang, A.-Y. Song, Y.-B. He, B.-H. Li, Z.-Q. Lin, *J. Mater. Chem. A* **2015**, 3, 13340–13349.
- [12] J. Wang, Z.-Q. Lin, *Chem-Asian J.* **2012**, 7, 2754–2762.
- [13] X.-Y. Li, L.-H. Chen, Y. Li, J.-C. Rooke, C. Wang, Y. Lu, A. Krief, X.-Y. Yang, B.-L. Su, *J. Colloid Interface Sci.* **2012**, 368, 128–138.
- [14] Y. Li, S. Wang, Y.-B. He, L.-K. Tang, Y. V. Kaneti, W. Lv, Z.-Q. Lin, B.-H. Li, Q.-H. Yang, F.-Y. Kang, *J. Mater. Chem. A* **2017**, 5, 4359–4367.
- [15] X. Lu, F. Huang, X. Mou, Y. Wang, F. Xu, *Adv. Mater.* **2010**, 22, 3719–3722.
- [16] L.-H. Chen, X.-Y. Li, G. Tian, Y. Li, H.-Y. Tan, G.-V. Tendeloo, G.-S. Zhu, S.-L. Qiu, X.-Y. Yang, B.-L. Su, *ChemSusChem* **2011**, 4, 1452–1456.
- [17] X.-Y. Yang, S.-B. Zhang, Z.-M. Qiu, G. Tian, Y.-F. Feng, F.-S. Xiao, *J. Phys. Chem. B* **2004**, 108, 4696–4700.
- [18] D. Wu, Y. Wang, H. Dong, F. Zhu, S. Gao, K. Jiang, L. Fu, J. Zhang, D. Xu, *Nanoscale* **2013**, 5, 324–330.
- [19] W.-Q. Fang, J.-Z. Zhou, J. Liu, Z.-G. Chen, C. Yang, C.-H. Sun, G.-R. Qian, J. Zou, S.-Z. Qiao, H.-G. Yang, *Chem. Eur. J.* **2011**, 17, 1423–1427.
- [20] J. S. Chen, Y.-L. Tan, C.-M. Li, Y.-L. Cheah, S. Madhavi, F.-Y.-C. Boey, L. A. Archer, X. W. Lou, *J. Am. Chem. Soc.* **2010**, 132, 6124–6130.
- [21] Z.-K. Zheng, B.-B. Huang, X.-Y. Qin, X.-Y. Zhang, Y. Dai, *Chem. Eur. J.* **2010**, 16, 11266–11270.
- [22] B.-S. Li, B.-J. Xi, Z.-Y. Feng, Y. Lin, J.-C. Liu, J.-K. Feng, Y.-T. Qian, S.-L. Xiong, *Adv. Mater.* **2018**, 30, 1705788.
- [23] M.-Z. Ge, J.-S. Cai, J. Iocozzi, C.-Y. Cao, J.-Y. Huang, X.-N. Zhang, J.-L. Shen, S.-C. Wang, S.-N. Zhang, K.-Q. Zhang, Y.-K. Lai, Z.-Q. Lin, *Int. J. Hydrogen Energy* **2017**, 42, 8418–8449.
- [24] M.-Y. Wang, J. Iocozzia, L. Sun, C.-J. Lin, Z.-Q. Lin, *Energy Environ. Sci.* **2014**, 7, 2182–2202.
- [25] M. D'Arienzo, J. Carbajo, A. Bahamonde, S. Polizzi, R. Scotti, L. Wahba, F. Morazzoni, *J. Am. Chem. Soc.* **2011**, 133, 17652–17661.
- [26] H.-G. Yang, C.-H. Sun, S.-Z. Qiao, J. Zou, G. Liu, S.-C. Smith, H.-M. Cheng, G.-Q. Lu, *Nature* **2008**, 453, 638–641.
- [27] G. Wang, Y. Ling, Y. Li, *Nanoscale* **2012**, 4, 6682–6691.
- [28] S.-M. Wu, X.-L. Liu, X.-L. Lian, G. Tian, C. Janiak, Y.-X. Zhang, Y. Lu, H.-Z. Yu, J. Hu, H. Wei, H. Zhao, G.-G. Chang, G.-V. Tendeloo, L.-Y. Wang, X.-Y. Yang, B.-L. Su, *Adv. Mater.* DOI: <https://doi.org/10.1002/adma.201802173>.
- [29] D. Nakamura, I. Gunjishima, S. Yamaguchi, T. Ito, A. Okamoto, H. Kondo, S. Onda, K. Takatori, *Nature* **2004**, 430, 1009–1012.
- [30] X.-Y. Yang, L.-H. Chen, Y. Li, J. C. Rooke, C. Sanchez, B.-L. Su, *Chem. Soc. Rev.* **2017**, 46, 481–558.
- [31] X.-Y. Yang, Y. Li, L. Arnaud, J.-G. Yu, B.-L. Su, *Pure Appl. Chem.* **2009**, 81, 2265–2307.
- [32] D. Chen, L. Cao, F. Huang, P. Imperia, Y.-B. Cheng, R. A. Caruso, *J. Am. Chem. Soc.* **2010**, 132, 4438–4444.
- [33] R.-L. Liu, Y.-F. Shi, Y. Wan, Y. Meng, F.-Q. Zhang, D. Gu, Z.-X. Chen, B. Tu, D.-Y. Zhao, *J. Am. Chem. Soc.* **2006**, 128, 11652–11662.
- [34] Y.-Y. Wen, H.-M. Ding, Y.-K. Shan, *Nanoscale* **2011**, 3, 4411–4417.
- [35] Y. Chen, W. Li, J. Wang, Y. Gan, L. Liu, M. Ju, *Appl. Catal. B* **2016**, 191, 94–105.
- [36] S. Wang, L. Pan, J. J. Song, W. Mi, J. J. Zou, L. Wang, X. Zhang, *J. Am. Chem. Soc.* **2015**, 137, 2975–2983.
- [37] M. A. Rahman, S. Bazargan, S. Srivastava, X. Wang, M. Abd-Ellah, J. P. Thomas, N. F. Heinig, D. Pradhan, K. T. Leung, *Energy Environ. Sci.* **2015**, 8, 3363–3373.

---

Manuscript received: April 18, 2018  
 Revised manuscript received: June 16, 2018  
 Accepted manuscript online: June 21, 2018  
 Version of record online: August 7, 2018